



Characterization of Calcination Process of Electric Arc Furnace Dust with Lime: A Behavior of Zinc, Lead, and Iron

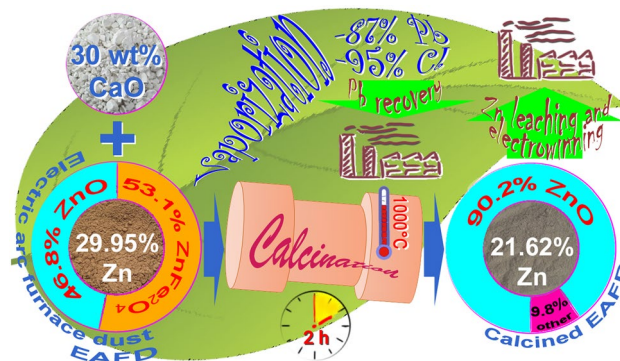
Pavel Grudinsky¹ · Denis Pankratov² · Valery Dyubanov¹ · Mikhail Sevostyanov¹

Received: 18 March 2022 / Accepted: 12 September 2022 / Published online: 28 September 2022
© The Minerals, Metals & Materials Society 2022

Abstract

A behavior of zinc, lead, and iron during the processing of EAFD (electric arc furnace dust from steelmaking) by the promising method based on its calcination with lime was studied. The chemical and mineralogical composition of the EAFD were analyzed in detail by X-ray fluorescence, X-ray diffraction, and Mössbauer analyses, as well as using methods of chemical phase analysis. It was found that EAFD contains 29.95% Zn consisting of 15.9% of ferrite and 13.81% of free oxide, as well as 0.77% Pb, which is mainly in silicate form. It was shown that calcination of EAFD with CaO in the mass ratio of 1:0.3 at 1000 °C for 120 min led to the conversion of 90.2% Zn into the highly soluble form of ZnO and the removal of 95% Cl and 87% Pb that resulted to obtaining the calcine suitable for further leaching and electrolysis in zinc plants. Based on the obtained thermodynamic, kinetic, and analysis data, the behavior of zinc, lead, and iron during the calcination was discussed.

Graphical Abstract



Keywords Electric arc furnace dust · Calcium oxide · Dicalcium ferrite · Waelz process · Zinc oxide · Zinc ferrite

Introduction

In 2020, total production of steel in the world was 1.878 billion tons of crude steel, 26.3% of which was obtained in electric arc furnaces [1]. Electric arc furnace dust (EAFD) is a by-product of electric steelmaking with high contents of zinc, lead, and iron. Electric arc smelting can produce about 15–25 kg of dust per ton of crude steel [2]. Currently, recycling proportion of generated dust is about 50% that leads to obtaining approximately 6% of all zinc produced in the world [3].

The contributing editor for this article was Dimitrios Panias.

✉ Pavel Grudinsky
GruPaul@yandex.ru

¹ A. A. Baikov Institute of Metallurgy and Materials Science, Russian Academy of Science, 119334 Moscow, Russia

² Lomonosov Moscow State University, 119991 Moscow, Russia

EAFD contains zinc both in the forms of hardly soluble ferrite (ZnFe_2O_4) and free highly soluble oxide (ZnO) [4]. There are also significant contents of chlorides [5] and sometimes fluorides [6] that hinder direct EAFD processing by hydrometallurgical zinc plants. The presence of zinc ferrite is undesirable due to a necessity for the application of additional stages of strong sulfuric acid leaching and iron precipitation after conventional weak sulfuric acid leaching [7]. Considerable contents of halogens require additional stages for their removal because they pass into the leaching solution and impede the further electrolysis process. Chlorine ions in the sulfate solutions cause corrosion of electrodes, increase energy consumption, and can also induce the release of gaseous chlorine, which deteriorates working conditions in the electrolysis plant [8]. Fluoride ions hamper stripping of electrolytic zinc from aluminum cathode [9–11]. Thus, to involve EAFD as a raw material for zinc production, its pretreatment is necessary to remove halogens and to decompose zinc ferrite.

In order to recycle EAFD with comprehensive extraction of valuable components, many authors have proposed various technologies using both pyrometallurgical [12] and hydrometallurgical methods [13]. The main EAFD recycling method is the Waelz process, which is pyrometallurgical processing of the dust in a rotary kiln with carbonaceous reducing agent [14]. At the present time, the Waelz process treats more than 85% of the EAFD involved in recycling [15]. In the Waelz process, carbothermic reduction at 1250–1300 °C decomposes ZnFe_2O_4 , so zinc evaporates and passes into zinc-rich Waelz oxide. The Waelz oxide also accumulates halogens, so the next treatment stage is used to remove them either by calcination at temperatures over 900 °C [16, 17] or by leaching with aqueous solutions of sodium carbonate [18, 19]. Despite the widespread prevalence of the Waelz process, its disadvantage is impossibility to avoid the second-stage treatment of the Waelz oxide. Moreover, considerable consumption of coke breeze in the range of 180–350 kg per ton of dust should be noted [20] that leads to significant CO_2 emission [21]. Currently, the global upcoming trends in industry is reduction of CO_2 emissions [22, 23] and development of carbon-neutral economy [24], so in the foreseeable future, the Waelz process probably can be substituted for other methods for EAFD recycling with low greenhouse gas emissions. Among many different approaches, EAFD calcination with lime [25–30] is noteworthy due to the possibility of rotary kiln application, like the Waelz process, but probably lower CO_2 emission compared with the one owing to a feasibility of the processing without coke breeze in the charge. It is important to note that decomposition of zinc ferrite and removal of halogens during the calcination of EAFD with lime occur within a single pyrometallurgical stage.

This research focuses on the in-depth investigation of zinc, lead, and iron behavior during EAFD calcination with

lime. The experiments were carried out to study the effect of temperature, calcination time, and lime amount on the decomposition of zinc ferrite, as well as on the behavior of other components of EAFD.

Materials and Methods

Thermodynamic simulation was performed by HSC Chemistry 9.9 (Finland) software [31] using Equilibrium Composition module. The calculation was carried out per 100 kg of EAFD at temperature range of 600–1100 °C using gas phase containing 20% O_2 + 80% N_2 and model composition of the dust based on the results of chemical and phase analyses. It was assumed that all phases are pure substances with activity of 1.

The EAFD sample containing 29.95% Zn and 0.77% Pb, as well as reagent grade CaO, was used in the experiments. CaO was preliminary calcined at 1000 °C for 2 h to remove residual calcium hydroxide and carbonate. EAFD and CaO were ground in an agate mortar up to the fraction of 0.2 mm and mixed in certain ratios by V-shell blender for 24 h. The mixtures were pressed into tablets with a pressure of 170 MPa; each tablet was 1 g in weight and 17 mm in diameter. 3 g of the mixture in corundum crucible was placed in a preheated muffle furnace at the temperature in the range of 800–1100 °C. Calcination time was in the range of 1–120 min. Selective leaching of zinc oxide from ferrite in calcined samples was carried out by aqueous solution of NH_4Cl + NH_4OH [32]. 2 g of the sample was placed in a flask containing 200 ml of the mixture prepared by 22 g NH_4Cl dissolution in 80 ml of NH_4OH with a density of 0.9 g/cm³ and 120 ml of water. The solution was stirred at 50–60 °C for 2 h and filtered out. The residue was flushed out 4–6 times by 1% NH_4Cl solution, then heated up to 50 °C, and flushed out 2–3 times by hot water. The obtained calcined samples and the ammonia-chloride solutions were analyzed by atomic emission spectroscopy with inductively coupled plasma (ICP-OES) by Agilent 725 (USA) device.

The chemical composition of the dust was analyzed by the atomic emission spectrometer Agilent 725 (USA) (Zn, Pb, Fe contents), LECO CS-400 (USA) device (carbon content), and X-ray fluorescence spectrometer ARL QUANT'X (Switzerland) (the rest elements). Chlorine in the calcined samples was determined by argentometric titration and turbidimetric methods [33]. Fluorine in the EAFD sample was analyzed by potentiometric titration using the state standard GOST 14048.7–80. The XRD patterns were obtained by X-ray diffractometer ARL X'TRA (Switzerland) using Cu-K_α radiation.

Phase composition of the samples was determined using original software. The software algorithm was based on matching the experimental XRD pattern and the entries

from the ICCD PDF [34] and COD [35] databases by varying intensity, width and shape of the peaks. The ICCD and COD data were used "as is": without changing the number, position, and relative intensity of peaks. The criteria for the satisfactory matching the experimental XRD pattern were the minimum standard deviation of the model from the experimental data, the correspondence of the composition and number of components for the chemical model, and the feasibility of the obtained set of variable parameters for the physical model. The semi-quantitative analysis of the components was assessed by the Reference Intensity Ratio (RIR) method using their I/I_{cor} from the databases.

Mössbauer absorption spectra were obtained by Mössbauer spectrometer MS1104EM (Russian Federation). The γ -radiation source was 13 mCi ^{57}Co in a matrix of metallic Rh. The spectra were collected at room temperature (296 ± 3 K) and at liquid nitrogen temperature (77.5 ± 0.5 K) until the noise/signal ratio reaches 1 or 2%. The experimental data processing was carried out for Mössbauer spectra of high resolution (1024 points) using the SpectRelax 2.8 software (Russian Federation). In the case of the processing using a model, the spectra were fitted by combinations of symmetrical doublets and sextets with controlled ratios of the intensity and width of the resonance lines. Values of chemical shift are given relative to $\alpha\text{-Fe}$.

Particle size distribution in the samples was analyzed by laser light diffraction method using Fritsch Analysette 22 Next Nano (Germany) device.

To specify the zinc and lead phase distribution, methodology of chemical phase analysis was applied that described in detail in [32]. Figure 1a and b demonstrates two particular flowsheets for the selective dissolution of different zinc and lead phases, respectively.

A polished section was prepared to examine the calcined EAFD sample by the methods of optical microscopy (OM) and scanning electron microscopy (SEM). A reflected-light optical microscope METAM LV-34 (Russia) and a camera RisingCam RT5109 (China) were used to snap photomicrographs of the polished section. The sample was also analyzed using scanning electron microscope Tescan VEGA 3SB (Czech Republic) and energy-dispersive X-ray analyzer (EDX) INCA SDD X-MAX (United Kingdom).

Results

EAFD Characterization

Table 1 shows chemical composition of the EAFD sample.

Figure 2 illustrates the XRD pattern of the EAFD sample; Table 10 in Appendix lists the quantitative composition of the sample using RIR method with the marked entry numbers of the identified phases in the XRD databases.

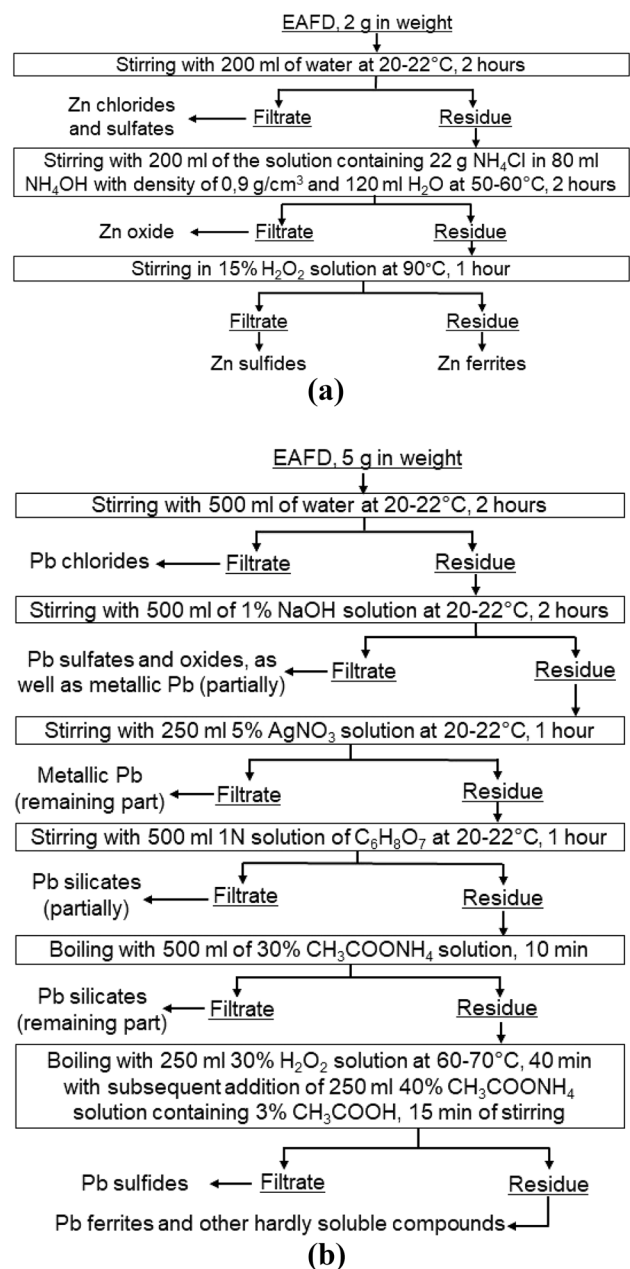
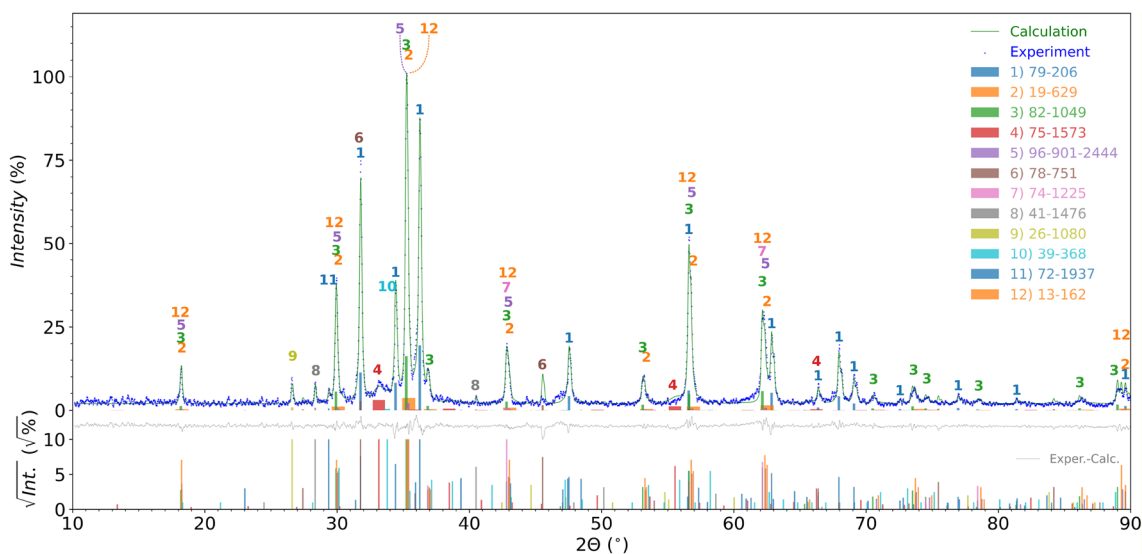


Fig. 1 The flowsheets of chemical phase analysis of Zn (a) and Pb (b) phases in EAFD

The results indicate that the main minerals in the EAFD sample are ZnFe_2O_4 and ZnO . Furthermore, considerable contents of NaCl and KCl are present, which are likely the major halogen compounds of the sample. A certain percentage of charge materials of electric steelmaking such as CaCO_3 and C are detected. The other identified phases are oxides and silicates such as Mn_3O_4 , Fe_3O_4 , FeMnO_3 , and $\text{Ca}_3\text{Al}_2(\text{SiO}_4)_3$. The presence of amorphous phases is clear due to an amorphous ring existence at $2\theta = 28\text{--}40^\circ$.

Table 1 Chemical composition of the EAFD sample, wt%

Zn	Fe	Pb	Al	Si	Ca	Mg	Na	K	Mn	Cr	Cu	Cl	F	C	P	S
29.95	21.37	0.77	0.28	1.2	5.34	0.71	0.85	1.37	1.53	0.11	0.10	1.21	<0.01	2.0	0.06	0.70

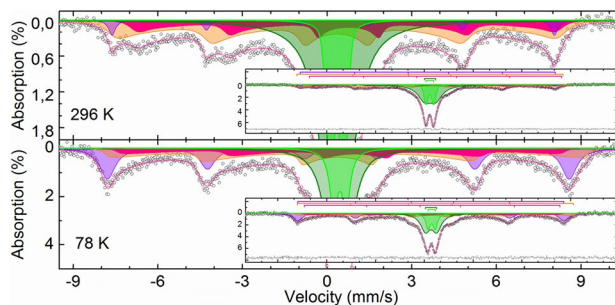
**Fig. 2** XRD pattern of EAFD, where (1) ZnO, (2) Fe₃O₄, (3) ZnFe₂O₄, (4) FeMnO₃, (5) Cu_{0.4}Zn_{0.6}Fe₂O₄, (6) NaCl, (7) MgO, (8) KCl, (9) C, (10) Ca₃Al₂Si₃O₁₂, (11) CaCO₃, (12) Mn₂O₄ are identified (entry numbers in the legend are given from the ICDD and COD databases)**Table 2** Distribution of zinc and lead minerals in the EAFD sample

Zn phases	Content in the EAFD sample, wt%	Distribution, rel. %	Pb phases	Content in the EAFD sample, wt%	Distribution, rel. %
Chlorides + sulfates	0.01	0.04	Chlorides	0.006	0.76
Oxide	14.02	46.80	Oxide + sulfate + metal	0.13	16.50
Sulfide	0.02	0.06	Silicates	0.58	75.60
Ferrites	15.9	53.10	Sulfide	0.003	0.39
			Ferrites + other hardly soluble phases	0.05	6.75

Table 2 shows the results of chemical phase analysis of zinc and lead minerals.

The obtained data demonstrate that zinc content both as chlorides and as sulfides is insignificant; the main zinc-containing phases are ferrite and oxide in approximately equal proportion. As in the case of zinc, the lead content in the chloride and sulfate form is negligible, but major phases are distributed differently. Most of the lead is in silicate form, but some amounts of sulfates, oxides, metal, and ferrites are also present.

Figure 3 depicts the Mössbauer spectra of EAFD collected at the both temperatures; Table 3 lists values of its parameters. They involve an intense and wide doublet, as well as a poorly resolved combination of broad and low-intensity resonance lines of a distorted sextet. The spectrum obtained at 78 K has a relatively high intensity and

**Fig. 3** Mössbauer spectra of the EAFD sample obtained at 296 and 78 K, as well as models for their description

symmetry, while the spectrum obtained at 298 K is asymmetric, not so high intensity, and is clearly a superposition of

Table 3 Parameters of the Mössbauer spectra of the EAFD sample

Temperature, K		296							78						
Phase	Site	#	δ^*	$\Delta = 2\varepsilon$	Γ_{exp}	α	H_{hf}	S#	δ	$\Delta = 2\varepsilon$	Γ_{exp}	α	H_{hf}	S#	
			mm/s	–	kOe	%	mm/s	–	kOe	%					
$\text{Cu}_{1-x}\text{Zn}_x\text{Fe}_2\text{O}_4$	$\text{Fe}^{3+}_{\text{Th}}$	1	0.24	– 0.04	0.29		486.3	2.9	0.45	– 0.10	0.66		507.6	22	
$\text{Fe}_{3-\delta}\text{O}_4$	$\text{Fe}^{3+}_{\text{Th}}$	2	0.34	0.01	0.46	2.2	507	27	0.53	0.31	0.30	1.8	526	26	
$\text{Fe}_{3-\delta}\text{O}_4$	$\text{Fe}^{2.5+}_{\text{Oh}}$	3	0.72	– 0.07	0.25	2.2	481	14	0.74	– 0.50	0.3	1.8	487	16	
$\text{Cu}_{1-x}\text{Zn}_x\text{Fe}_2\text{O}_4, \text{FeMnO}_3$	$\text{Fe}^{3+}_{\text{Oh}}$	4	0.356	0.68	0.98			41	0.418	0.70	0.70			26	
ZnFe_2O_4	$\text{Fe}^{3+}_{\text{Oh}}$	5	0.344	0.470	0.32			15	0.449	0.44	0.32			11	

* δ – isomer shift, $\Delta = 2\varepsilon$ – quadrupole splitting, $\alpha = (KV)/(k_B T)$ – ratio of particle anisotropy energy to thermal energy (K – magnetic anisotropy constant, V – domain volume, k_B – Boltzmann's constant, T – temperature), Γ_{exp} – line width, H_{hf} – hyperfine magnetic field, and S# – relative area of a subspectrum #

several subspectra. A strong temperature dependence of both the intensity and the profile indicates that components in the superparamagnetic state are present in the EAFD sample. The change in the symmetry of the ferromagnetic part of the spectra is a characteristic behavior of magnetite.

Most of the ferromagnetic part of the spectra can be described using the many-state superparamagnetic relaxation model [36] by two sextets with a single set of relaxation parameters (Table 3, ##2–3). The Mössbauer parameters of these sextets correspond to Fe^{3+} atoms in tetrahedral voids and $\text{Fe}^{3+}/\text{Fe}^{2+}$ atoms in octahedral voids of the spinel-type crystal lattice [37]. In particular, the hyperfine parameters are hybrid between the isostructural magnetite and maghemite [38], which suggest that the subspectra are related to partially oxidized magnetite $\text{Fe}_{3-\delta}\text{O}_4$ [39, 40]. It should be noted that magnetite and maghemite, as well as their solid solutions, are isostructural and almost indistinguishable in XRD patterns. If we assume that the sample particles have a spherical shape and the value of the magnetic anisotropy constant at room temperature is 10^5 J/m^3 , which is equivalent to the average value for nanosized maghemite and magnetite [41, 42], the size of the corresponding magnetic domains is estimated at the level of about 5.5 nm. It is consistent with a noticeable broadening of the diffraction peaks for the corresponding phase in the XRD pattern (Fig. 2).

The rest of ferromagnetic part of the spectra is the sextet (Table 3, #1) which is probably a substance related to copper ferrite [43], namely, the substituted copper ferrite $\text{Cu}_{1-x}\text{Zn}_x\text{Fe}_2\text{O}_4$ [44, 45]. The subspectrum area significantly increases with decreasing the collecting temperature, which can be associated with ferrimagnetic interactions between ferrimagnetic nanoparticles of inhomogeneous composition distributed over the diamagnetic matrix of the composite. Apparently, the mentioned area change of the subspectrum #1 with the temperature shift occurs simultaneously with the outer most intense and wide doublet #4 (Table 3), which is one of the two describing the paramagnetic part of the Mössbauer spectra. Therefore, one can assume that this doublet

partially describes copper ferrites with a high substitution degree of copper by zinc and T_c (Curie point) in the studied temperature range [46]. On the other hand, it should be noted that this subspectrum is likely a compound doublet. It can include another doublet with similar parameters close to FeMnO_3 , which has T_c below the nitrogen boiling point [47–49]. A substantial width of the corresponding resonance lines even at 78 K indicates a low crystallinity of this phase, which agrees well with the XRD pattern (Fig. 2), where the corresponding peaks are also significantly broadened.

The second doublet, which has the significantly smaller values of the quadrupole splitting and the line width, corresponds to zinc ferrite ZnFe_2O_4 [50, 51]. The relatively narrow resonance lines for this doublet are consistent with a low width of the XRD peaks that indicate a high crystallinity of the corresponding phase.

Thermodynamic Simulation

Based on the results of chemical and phase analysis without taking into account components of low contents, initial EAFD composition for the simulation was accepted as follows: wt%: 58.69 ZnFe_2O_4 ; 17.47 ZnO ; 2.34 $\text{Ca}_3\text{Al}_2\text{Si}_3\text{O}_{12}$; 1.18 MgO ; 0.38 CuFe_2O_4 ; 4.20 CaO ; 4.29 CaCO_3 ; 2.61 KCl ; 2.16 NaCl ; 1.49 C ; 0.30 Fe_3O_4 ; 1.55 SiO_2 ; 1.65 Mn_3O_4 ; 0.61 Mn_2O_3 ; 0.16 Cr_2O_3 ; 0.71 Pb_2SiO_4 ; 0.10 PbO ; 0.06 PbSO_4 ; 0.05 Pb . Figure 4 shows the results of thermodynamic simulation of equilibrium states.

The thermodynamic simulation has evidenced that the main reaction of zinc ferrite decomposition is interaction with the formation of dicalcium ferrite:

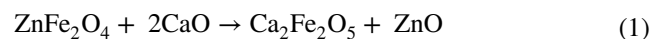


Figure 4a shows that in order to convert zinc into the highly soluble form completely, at least 26 wt% CaO should be added. Accordingly, in the preliminary experiments, a small excess of 30 wt% CaO addition was used.

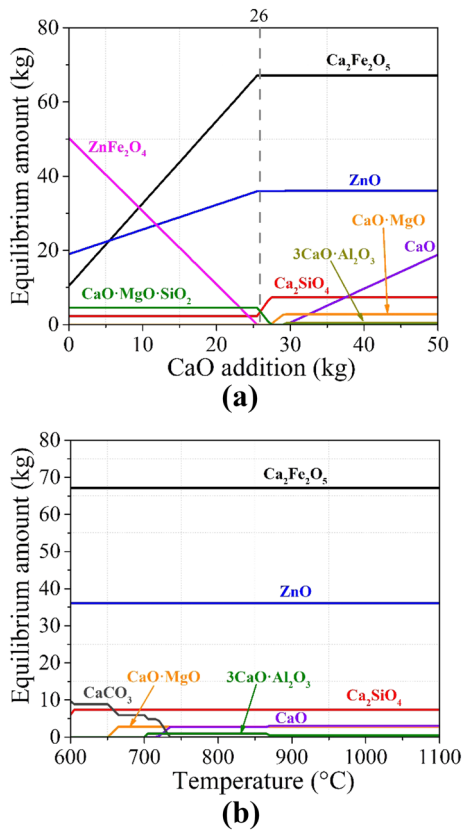


Fig. 4 Effect of CaO addition on equilibrium amounts of major zinc, iron, and calcium compounds in the dust at 1000 °C (a) and temperature dependence of equilibrium amounts of zinc and calcium compounds with addition of 30% CaO to 100% EAFD (b)

Chlorine Behavior

To define more accurately the required calcination temperature, a preliminary experimental study of chlorine behavior was carried out. To prevent the negative consequences of halogen influence, chlorine and fluorine should be removed from the calcine to the required level of <0.06% Cl and <0.01% F [52]. The EAFD sample has already complied with the requirements for fluorine content (Table 1), so we studied only the behavior of chlorine. Table 4 demonstrates the residual chlorine content in the calcined EAFD samples obtained during the experiments.

Table 4 Remaining chlorine content in the samples obtained by the calcination of EAFD+30% CaO at various temperatures and duration, wt%

Duration, min	Temperature, °C		
	800	900	1000
60	0.40	0.48	0.17
120	0.27	0.26	0.051

The results have indicated that to conform with the requirements for the chlorine content, the EAFD calcination is required at least at 1000 °C for 120 min. Based on these data, we chose duration of 1–120 min for further experiments.

Zinc Behavior

Figure 5 shows the influence of CaO amount and calcination time on zinc ferrite conversion into the oxide form.

It can be seen that the EAFD calcination without lime and with insignificant lime addition led to decreasing of zinc percentage in the highly soluble ZnO form (Fig. 5a) that is probably due to partial ferritization by the interaction of free zinc and iron oxides contained in the dust. At 20 wt% CaO addition to EAFD, 87.7% of zinc was in ZnO form, while 30 wt% CaO addition resulted in 90.2% of zinc in ZnO form. Further increasing of CaO addition influenced the remaining zinc ferrite decomposition insignificantly.

Figure 4b demonstrates that the share of zinc in the highly soluble ZnO form at all chosen temperatures was in

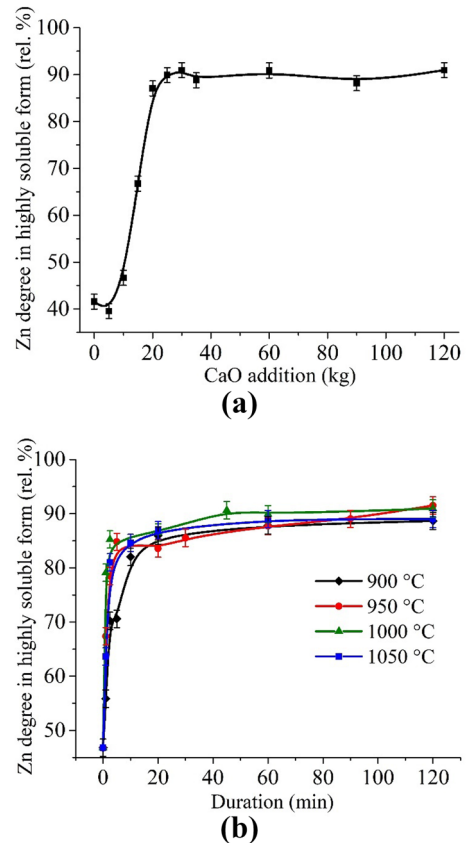


Fig. 5 Effect of CaO addition on the relative zinc percentage in the oxide form at 1000 °C after 60 min of the calcination (a) and calcination duration at 950–1050 °C with the addition of 30% CaO to 100% EAFD (b)

the range of 80–90% already after 10 min of calcination. It is noteworthy that the curves at all the temperatures are almost the same that is consistent with the other study [25]. Evidently, the best result was 90% of zinc in highly soluble ZnO form that was obtained at 1000 °C after 45 min of the calcination. Thus, to convert 90% of zinc into ZnO form, the EAFD calcination with 30 wt% CaO at 1000 °C for 45 min is quite sufficient. However, to remove also chlorine to the required level, it is necessary to increase the calcination time to 120 min.

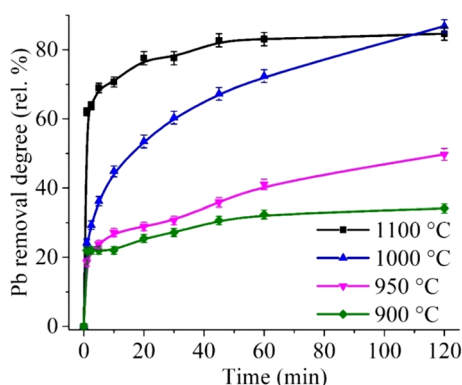


Fig. 6 Effect of calcination duration on lead vaporization from EAFD with 30% CaO at 900–1100 °C

Lead Behavior

Figure 6 shows the kinetic curves of Pb removal in the range of 900–1100 °C.

As can be seen, the Pb removal rate after the 120 min calcination is less than 30% at 900 °C and above 80% at 1000–1100 °C.

A rate-controlling step of Pb removal process in the range from 1 to 120 min was assessed by conventional model fitting of the experimental data with models based on different kinetic equations. Table 5 compares adequacy of the equations for the experimental data at different temperatures.

As follows from the listed data, the Jander equation gives the best fit to the Pb removal experimental curves that corresponds to the diffusion-controlled process. Figure 7a clearly demonstrates the adequacy of the Jander model at 900–1000 °C. Nevertheless, the Jander equation as the other models is in poor agreement with the experimental curve of 1100 °C.

The rate constants at different temperatures were evaluated from the appropriate slopes in Fig. 7a. Apparent activation energy was calculated using the logarithmic form of the Arrhenius equation:

$$\ln k = \ln A + \frac{E}{RT} \tag{2}$$

In the equation, E is the apparent activation energy (J/mol), k is the rate constant (min^{-1}), A is the preexponential factor (min^{-1}), R is the universal gas constant (8.314 J/

Table 5 Comparison of determination coefficient of several kinetic models for lead removal during calcination of the EAFD sample with CaO in the mass ratio of 100:30

Model Name	Integral Form $f(x)=k\tau$	T, °C	R ²	Model name	Integral Form $f(x)=k\tau$	T, °C	R ²
Jander	$[1 - (1 - x)^{1/3}]^2$	900	0.885	Erofeev-Avrami $n=3$	$[-\ln(1 - x)]^{1/3}$	900	0.838
		950	0.990			950	0.911
		1000	0.999			1000	0.880
		1100	0.754			1100	0.703
Hinstling-Brounstein	$1 - 2x/3 - (1 - x)^{2/3}$	900	0.882	Erofeev-Avrami $n=4$	$[-\ln(1 - x)]^{1/4}$	900	0.835
		950	0.988			950	0.903
		1000	0.990			1000	0.863
		1100	0.730			1100	0.699
Shrinking sphere	$1 - (1 - x)^{1/3}$	900	0.856	Chemical reaction of first order	$-\ln(1 - x)$	900	0.860
		950	0.955			950	0.964
		1000	0.941			1000	0.976
		1100	0.714			1100	0.740
Erofeev-Avrami $n=2$	$[-\ln(1 - x)]^{1/2}$	900	0.843	Chemical reaction of second order	$(1 - x)^{-1} - 1$	900	0.870
		950	0.927			950	0.982
		1000	0.911			1000	0.977
		1100	0.713			1100	0.809

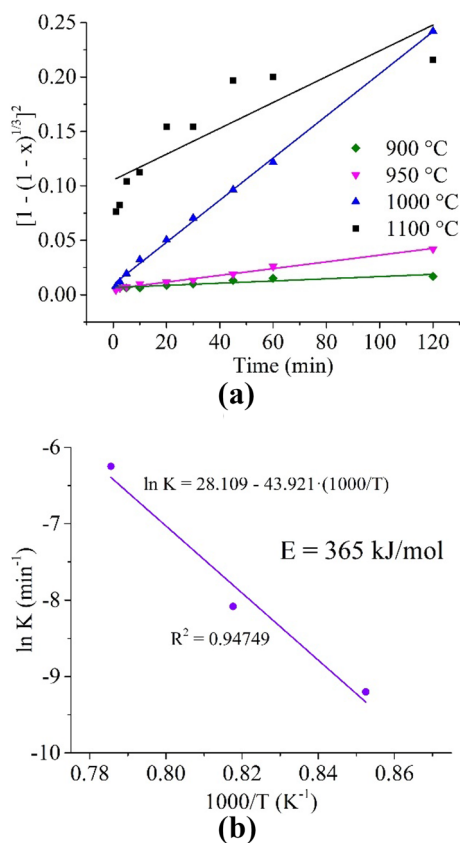


Fig. 7 Plot of Jander equation $F(x)=[1 - (1 - x)^{1/3}]^2$ vs. time at 900–1100 °C for Pb removal during the calcination of EAFD with 30% CaO (a) and Arrhenius plot for the process (b)

(mol·K)), T is the temperature (K), respectively. Figure 7b shows the results of determination of the apparent activation energy by the graphical method using the Eq. (2). Only the curves fitted to the Jander equation were taken into account, so the curve of 1100 °C was excluded from the calculation.

Correspondence of the Pb removal process with the Jander model agrees well with previously reported data [53], but the values of apparent activation energy differ by more than 2 times: 365 kJ/mol in our study vs. 175 kJ/mol in [53]. Taking into account lead mineralogy in the EAFD sample (Table 2), to elucidate the behavior of lead during the calcination, thermodynamic calculations were carried out using HSC Chemistry software. Figure 8a demonstrates the equilibrium amounts of Pb compounds at different temperatures during the calcination of EAFD.

As follows from the equilibrium calculation, there is only an amount of lead as PbO in the condensed phase; condensed PbO decreases and PbO_(g) increases with a temperature rise over 850 °C. Moreover, above 1000 °C, the gas phase contains small amounts of lead chloride and metallic lead vapors.

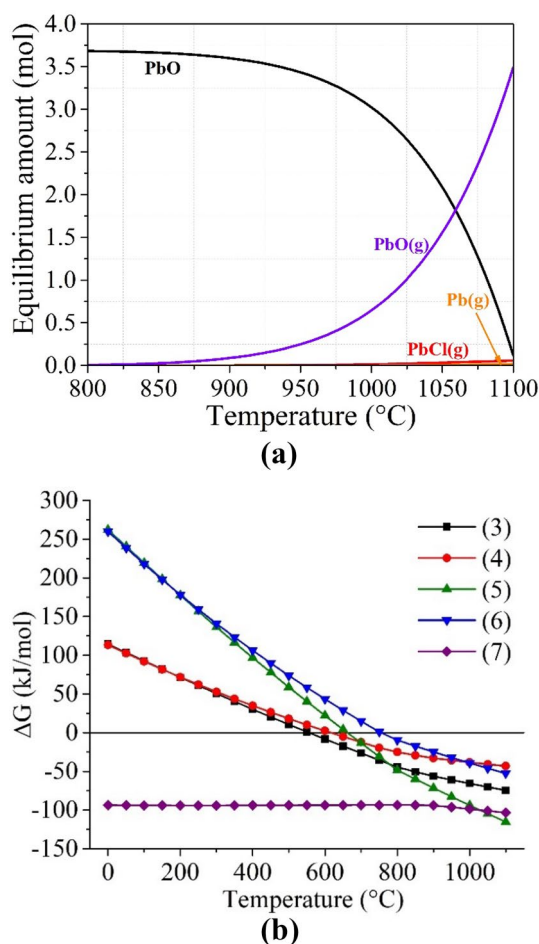
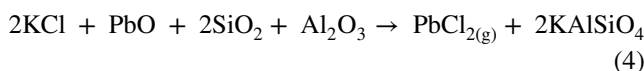
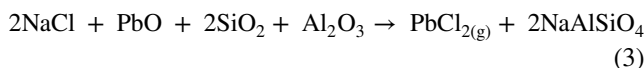


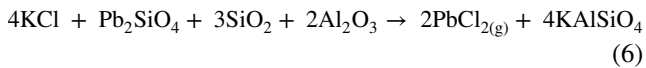
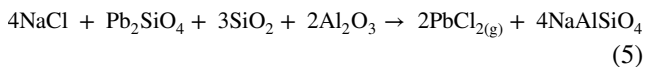
Fig. 8 Temperature dependence of equilibrium amounts of lead compounds with addition of 30% CaO to 100% EAFD (a) and temperature dependence of the Gibbs free energy change of the reactions (3–7) (b)

Probably, lead components, which were detected by chemical phase analysis (Table 2), during the EAFD calcination behaves as follows. A small amount of lead chloride contained in the dust vaporizes already during the heating up to the required temperature [54]. Lead sulfide interacts with atmospheric oxygen to form oxysulfates and sulfates [55] and then the oxysulfates and the sulfate already contained in the dust in the range of 800–1000 °C decompose stepwise to oxide according to the scheme [56, 57]: $\text{PbSO}_4 \rightarrow \text{PbO} \cdot \text{PbSO}_4 \rightarrow 2\text{PbO} \cdot \text{PbSO}_4 \rightarrow 4\text{PbO} \cdot \text{PbSO}_4 \rightarrow \text{PbO}$.

It is reported that the removal of lead oxide from EAFD can occur through interaction with chlorides by the following reactions [53]:



Similar reactions are likely to be possible for silicates, which are the main lead phases in EAFD in this study:



Lead silicate can react with lime to form PbO:

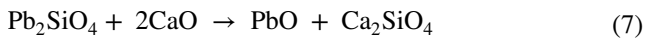


Figure 8b shows free Gibbs energy change of the reactions (3–7) at varied temperature. The presented data indicate that the reactions (3–7) are possible from 600 to 750 °C and above; the reaction (5) is the most thermodynamically probable at temperatures over 800 °C among the chlorination reactions. However, the reaction (7) is more probable than the reactions (3–6), so PbO is likely formed from lead silicate that is confirmed by the thermodynamic simulation (Fig. 8a).

Thus, based on the previous calculations, one might assume that the main part of lead during the EAFD calcination transforms into PbO and vaporizes as $\text{PbO}_{(\text{g})}$. It is supported by the fact that lead oxide has a significant vapor pressure at temperatures above 950 °C [58, 59] that is consistent with our experimental data (Fig. 6). In addition, a different evaporation condition compared with [53] is likely explained by the twofold value of apparent activation energy (Fig. 7b).

However, it is noteworthy that from 18 to 24 rel.% Pb has been already vaporized at 900–1000 °C during the heating and within the first minute of the holding, while at 1100 °C, this value is 62% (Fig. 6). Consequently, the chlorination of a certain part of lead by the reactions (3–6) and its evaporation in the chloride form during the calcination of EAFD is also possible. This assumption is confirmed by authors [60, 61], who has found out a high rate of Pb removal as lead chlorides at the temperature range of our study, as well as a possibility of lead vaporization at the temperatures even below 850 °C. After the main part of chlorides contained in the EAFD has been vaporized, a lead evaporation mechanism is also changed. This also explains a discrepancy between the experimental curve at 1100 °C and the kinetic models because a major part of lead was removed during the heating by the chlorination mechanism; then the rest was evaporated during holding as $\text{PbO}_{(\text{g})}$. The mechanism change is also confirmed by the more negative value of the

Gibbs free energy change of the chlorination reaction (5) than the reaction (7) above 1000 °C. This observation is of practical importance because the addition of chlorides to EAFD can increase the rate and reduce the temperature of the Pb removal.

It can be inferred from the obtained data that a temperature above 1000 °C is favorable for Pb removal from EAFD. Temperature of 1000 °C and the calcination duration of 120 min are the experimental conditions of best results for 87% Pb removal. It creates an opportunity to obtain during the calcination an intermediate product that can be used in lead production.

Calcined EAFD Characterization

Table 6 shows chemical composition of the calcined EAFD sample at the optimal calcination conditions.

Figure 9 illustrates the XRD pattern of the calcine obtained at optimal conditions. Table 11 lists the quantitative composition of the sample using RIR method with the marked entry numbers of the identified phases in the XRD databases.

XRD analysis has confirmed that the main part of zinc transforms into ZnO during the calcination according to reaction (1). The peaks are quite narrow due to high temperature treatment. The main iron-containing phase is dicalcium ferrite with a substitution of iron by different minor elements. An inconsiderable part of CaO remains unreacted that led to formation of complex carbonates probably during an air storage between cooling of the calcined EAFD sample and XRD analysis. There is a small amorphous ring on the XRD pattern; therefore, amorphous phases are present in the calcined EAFD.

It is notable that particle size of the calcined EAFD sample was increased compared to the initial EAFD sample. If the EAFD sample contains 31.7% particles < 1 μm and 82.7% particles < 10 μm, these values for the calcined EAFD sample grinded up to less 200 μm are 3.5% and 47.8%, respectively.

Figures 10 and 11 depict the Mössbauer spectra of the calcined EAFD with 30 wt% CaO and without CaO addition, respectively; Tables 7 and 8 list values of their parameters.

The Mössbauer spectrum of the sample calcined at 1000 °C without the addition of CaO is a doublet that is a superposition of two subspectra for high-spin Fe^{3+} in an octahedral oxygen environment (Fig. 11, Table 8). Hence, this spectrum has confirmed the occurrence of additional

Table 6 Chemical composition of the calcined EAFD sample with the addition of 30% CaO at 1000 °C for 120 min, wt%

Zn	Fe	Pb	Al	Si	Ca	Mg	Na	K	Mn	Cr	Cu	Cl	C	P	S
21.62	19.65	0.09	0.26	1.18	17.42	0.64	0.69	0.80	1.20	0.10	0.08	0.05	0.16	0.053	0.45

Fig. 9 XRD pattern of calcined EAFD with 30% CaO at 1000 °C for 120 min, where (1) ZnO, (2) $\text{Ca}_2\text{Fe}_{1.7}\text{Zn}_{0.15}\text{Si}_{0.15}\text{O}_5$, (3) $\text{Ca}_2\text{Fe}_2\text{O}_5$, (4) $\text{Ca}_2\text{Cr}_{0.5}\text{Fe}_{1.5}\text{O}_5$, (5) $\text{CuCr}_{1.7}\text{Mn}_{0.3}\text{O}_4$, (6) CaO, (7) $\text{Ca}(\text{Fe,Mg})(\text{CO}_3)_2$ (8) $(\text{Mn}_{2.58}\text{Fe}_{0.34}\text{Ca}_{0.08})(\text{Al}_{1.99}\text{Fe}_{0.01})\text{Si}_3\text{O}_{12}$, (9) Ca_2SiO_4 , (10) K_2CaSiO_4 are identified (entry numbers in the legend are given from the ICDD and COD databases)

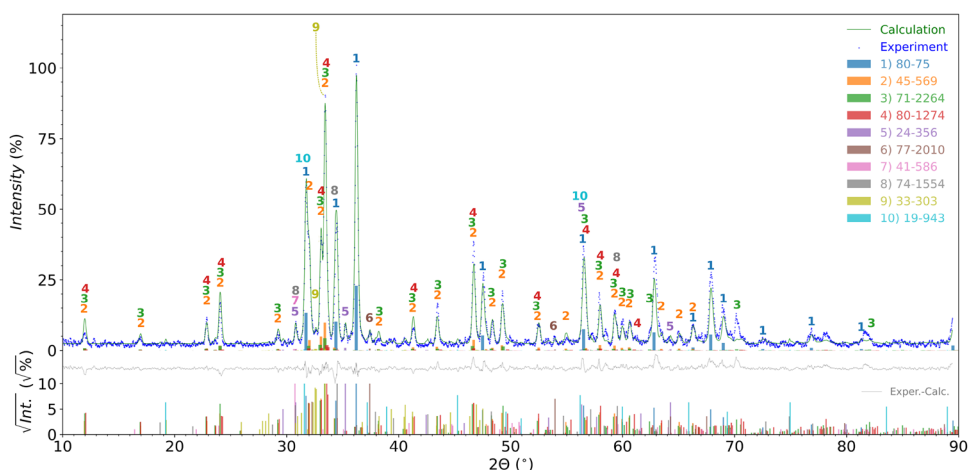


Fig. 10 Mössbauer spectra of the calcined EAFD sample with 30% CaO at 1000 °C for 120 min, models for their description, and the corresponding hyperfine magnetic field probability distribution functions

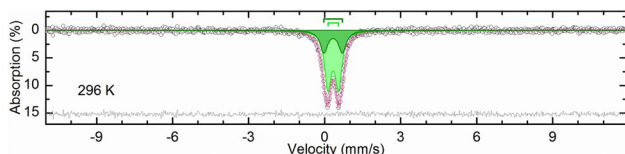
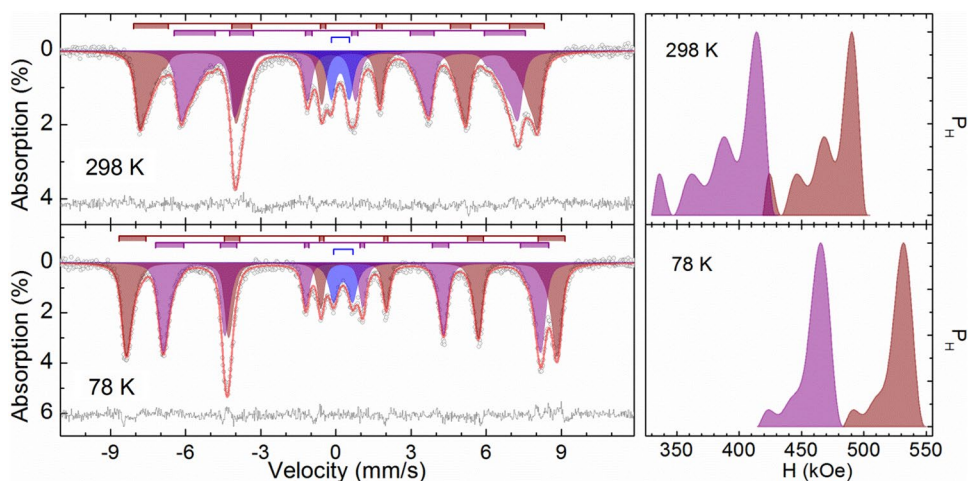


Fig. 11 Mössbauer spectra of the calcined EAFD sample at 1000 °C for 120 min without CaO addition and models for their description

ferritization of various elements including Zn during calcination without CaO (Fig. 5a). Therefore, one can assume that all changes in the Mössbauer spectra after the EAFD calcination with CaO are associated only with the formation of calcium-iron compounds. As follows from the spectra, they consist of more than ten resonance lines of different width and intensity. Moreover, the resonance lines in the outer part of the spectrum obtained at room temperature have a significant width and a distortion toward to the inner part of the spectrum. However, the resonance lines for the spectrum obtained at 78 K have a quite symmetry shape, a reduced line width, and a doubled intensity. Such an effect

of the temperature indicates the presence of iron compounds with a complex poorly ordered magnetic structure in the sample. Accordingly, the main part of spectra is two sextets, which described by similar hyperfine magnetic field probability distribution functions with the same area of the subspectra. It can be stated clearly that the corresponding subspectra describe the belonging of iron atoms to the same phases, moreover, in a ratio of 1:1. According to the values of parameters (Table 6), the sextets are related to dicalcium ferrite derivatives [62–65] with the brownmillerite structure [66, 67]. The distinction of iron compounds in this structural type is the placement of Fe^{3+} atoms in two different crystallographic positions with octahedral and tetrahedral oxygen environments, respectively [68]. Another distinguishing feature is high values of the quadrupole splitting of both the subspectra that require taking into account the quadrupole interaction constant to the second order of perturbation theory expressed by the parameters a_+ and a_- [69–71]. For this sample, the a_+/a_- ratio is -1, which corresponds to the value of the polar angle between V_{zz} and the direction of the internal magnetic field $H_{\text{hf}} \theta = 90^\circ$ as in the paper [72]. Appendix

Table 7 Parameters of the Mössbauer spectra of the calcined EAFD sample with 30% CaO at 1000 °C for 120 min

Temperature, K	296							78							
	Phase	Site	#	δ^*	$\Delta = 2\varepsilon$	Γ_{exp}	$a_+ = -a_-$	H_{ext}	S#	δ	$\Delta = 2\varepsilon$	Γ_{exp}	$a_+ = -a_-$	H_{ext}	S#
				mm/s				kOe	%	mm/s				kOe	%
Ca ₂ M _x Fe _{2-x} O ₅ , M are likely Al ³⁺ , Cr ³⁺ and Mn ³⁺	Fe ³⁺ _{Oh}	1	0.360	-0.483	0.331	-0.054	490.4	45.9	45.9	0.476	-0.469	0.315	-0.038	532.0	45.5
							469							509	
							447								
							424.7							492	
	Fe ³⁺ _{Th}	2	0.188	0.711	0.352		414.2	45.9	45.9	0.291	0.704	0.325		465.6	45.5
							388.3							443	
							362.44								
							336.45							424.0	
Si- and Al-oxide glass	Fe ³⁺ _{Th}	3	0.180	0.719	0.41			8.2	8.2	0.291	0.761	0.446			9.0

* δ – isomer shift, $\Delta = 2\varepsilon$ – quadrupole splitting, a_{\pm} – terms for taking into account the quadrupole interaction constant in the second order of perturbation theory, Γ_{exp} – line width, H_{ext} – hyperfine magnetic field for extremum of mode distribution functions, and S# – relative area of a subspectrum #.

Table 8 Parameters of the Mössbauer spectra at 296 K of the calcined EAFD sample at 1000 °C for 120 min without CaO addition

Phase	Site	#	δ^*	$\Delta = 2\varepsilon$	Γ_{exp}	S#
			mm/s			%
ZnFe ₂ O ₄	Fe ³⁺ _{Oh}	1	0.339	0.42	0.32	69
FeMnO ₃	Fe ³⁺ _{Oh}	2	0.336	0.73	0.36	31

* δ – isomer shift, $\Delta = 2\varepsilon$ – quadrupole splitting, Γ_{exp} – line width, and S# – relative area of a subspectrum #

(Table 12, Fig. 13) contains more rigorous description of the spectra in terms of full diagonalization of hyperfine Hamiltonian without any change in the given conclusion.

Hyperfine magnetic field probability distribution function illustrated in Fig. 10 for the both temperatures are trimodal at least (the leftmost mode observed in the spectra at room temperature can obviously be ignored due to the border effect). Evidently, the sample contains a number of solid solutions based on dicalcium ferrite Ca₂M_xFe_{2-x}O₅, which are mainly different in a decrease of hyperfine magnetic field value with an increase in the proportion (x) of impurity cations (M³⁺) substituting Fe³⁺ atoms in both sublattices [73, 74]. Probably, different modes in the probability distribution functions are related to different impurity compositions of dicalcium ferrite. These impurities must obey the rules of isomorphic substitution [75]; according to the data on the chemical composition of the sample (Table 6), they are likely Al³⁺, Cr³⁺, and Mn³⁺ [76–79]. The rest of the spectra is a doublet with a high values of quadrupole splitting and isomeric shift, which corresponds to Fe³⁺ atoms in a tetrahedral oxygen environment [80]. Due to the absence of corresponding iron-containing compound in the XRD pattern, the doublet is likely to be related to an amorphous phase. The values of the parameters suggest that it is a composite based on potassium-silicon glass phase with a low glass point with a high content of potassium or calcium–aluminum glass with

a low content of calcium or a combination of the both ones [81, 82], where Fe³⁺ atoms substitute Si⁴⁺ and Al³⁺ in tetrahedral positions, respectively, to form a solid solution.

Figure 12 shows photomicrographs of the calcined EAFD with 30 wt% CaO obtained using optical and scanning electron microscopy, respectively. Table 9 lists the composition of some points of SEM image, which are indicated in Fig. 12b.

The microscopy methods have pointed out that the calcined EAFD consists of a dicalcium ferrite base with zinc oxide and dicalcium silicate impregnation. The EDX analysis of points of dicalcium ferrite area in the Fig. 12 detected Zn, Mn, Si, and Al besides Ca and Fe. It cannot be ruled out that a part of the impurities in the sample points 1A, 1B, and 1C is in other separate components, which may be accidentally detected due to essential spatial and depth resolution of EDX analysis [83]. However, taking into account quite stable qualitative composition of these and other dicalcium ferrite points, XRD pattern (Fig. 9), which involves 3 various dicalcium ferrite entries, as well as Mössbauer spectra parameters (Fig. 10; Table 7), we assume that dicalcium ferrite include Zn, Mn, Si, and Al as substitutional impurities.

Among the impurities of dicalcium ferrite, zinc deserves particular attention. According to Fig. 5, 90.2% Zn is in the form of ZnO. The Mössbauer analysis (Fig. 10; Table 7) suggests that there is no significant amount of iron in the

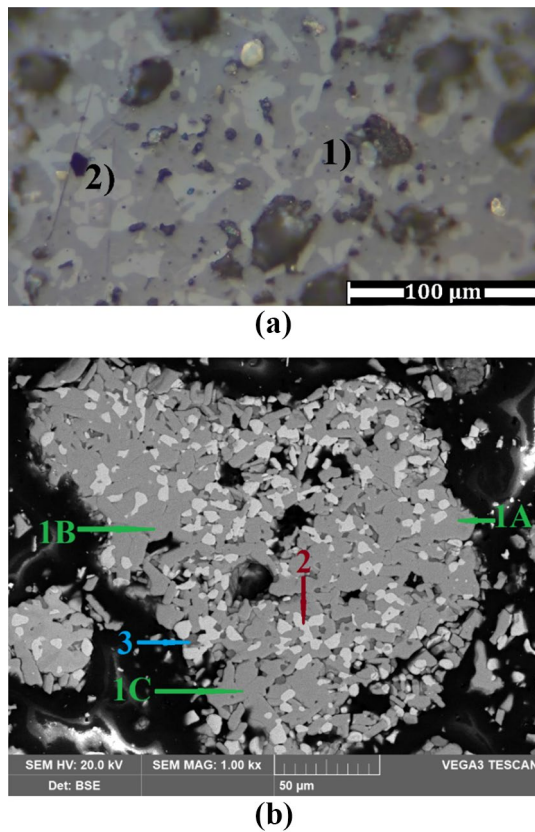


Fig. 12 OM (a) and SEM (b) images of the calcined EAFD with 30% CaO at 1000 °C for 120 min. The image (a) consists of dicalcium ferrite area 1) (dark gray) and zinc oxide area 2) (light gray). The elemental composition of marked points in the SEM image is in Table 9

zinc ferrite form in the calcined EAFD sample; the additional estimation resulted that less than 0.8% of iron can be potentially included in zinc ferrite. Hence, the cumulative evidence suggests that the rest of zinc is mainly a substitutional impurity of dicalcium ferrite that predetermines zinc losses in a residue during following leaching of the calcine.

Discussion

The study has shown that the EAFD calcination with 30 wt% CaO at 1000 °C for 120 min leads to the conversion of 90.2% Zn into highly soluble form and to the removal of 87% Pb, as well as of 95% Cl that is sufficient for the use of the calcined dust during further electrolysis. The only one required pyrometallurgical stage at relatively low temperatures with reduced fuel consumption is an undoubted advantage of this technology compared to the Waelz process. It is noteworthy that other papers [27, 28, 30], which studied the process on a laboratory scale, also achieved an incomplete zinc conversion into the oxide form at the level of about 90%. However, real dynamic calcination conditions in a rotary kiln, which are the better conditions for the interaction of solid phases compared to the static experimental ones, can increase the completeness of zinc transformation. In support of this assumption, the paper [84] has confirmed comparable to the Waelz process total zinc recovery of 95%, where the EAFD calcination technology with lime followed by alkaline leaching was tested in semi-industrial conditions for the production of zinc powder.

Touching upon greenhouse gas footprint of EAFD processing by the Waelz process and the calcination with lime, it is important to emphasize some points. The main sources for the CO₂ emissions for the approach based on the Waelz process are coke breeze combustion, flux (limestone or dolomite) decomposition, and gas fuel combustion at the Waelz oxide treatment stage to remove halogens (if applicable). It is notable that coke breeze in the Waelz process is indispensable because it is not only fuel and reducing agent, but also prevents charge melting and incrustation in a rotary kiln [14]. As for the approach based on the calcination with lime, CO₂ emissions not only from gas fuel combustion during the processing should be taken into account, but also from carbonate decomposition and gas fuel combustion during the production of lime from limestone. The conventional gaseous fuel used in the mentioned processes is natural gas, which is combusted with the lowest CO₂ emissions of all fossil fuels at about 15 kg C/GJ compared to coke breeze with about 29 kg C/GJ [85]. Evidently, because of a similarity of the processing conditions for the EAFD calcination with lime and the lime production from limestone, to reduce

Table 9 The elemental composition of points indicated in Fig. 12(b) obtained by EDX analyzer

Point	Content, wt%							
	Ca	Fe	Zn	O	Mg	Mn	Si	Al
1A	27.3	31.2	4.8	34.5	–	1.7	0.5	–
1B	27.9	33.2	1.6	35.4	–	0.8	0.5	0.6
1C	27.2	30.9	3.3	36.8	–	0.8	0.4	0.6
2	1.2	1.0	76.5	19.5	1.8	–	–	–
3	42.3	–	–	43.1	–	–	14.6	–

Table 10 Characteristics of two approaches based on the Waelz process and the calcination with lime in a rotary kiln for the EAFD treatment

Feature	The Waelz process	The calcination with lime
Processing temperature	1250–1300 °C	1000 °C
Fuel	Coke breeze with a possibility of minor partial substitution by a gaseous fuel	A gaseous fuel
Zinc behavior	Vaporizes and passes into the particular product (the Waelz oxide) as ZnO	Remains in the calcine product; about 90% transforms into ZnO
Lead behavior	Vaporizes and passes into the Waelz oxide	Vaporizes and passes into the sublimate
Sublimate product amount	About 30–40% of the charge feedstock	About 5% of the charge feedstock
Halogen removal stage	Required before or after (for the Waelz oxide) the processing	Not required; halogens are removed during the calcination
Zinc leaching stage	Applied for the halogen-free Waelz oxide, which is about 27–37% of the charge feedstock	Applied for the calcine, which is about 95% of the charge feedstock
Versatility	Suitable for EAFD and other various Zn-containing materials of different charge component ratio and zinc speciation	Suitable for EAFD; not tested for other Zn-containing materials

energy costs and CO₂ emissions, these two processes should be combined, i.e., EAFD can be calcined with limestone at once; such method invites further investigations.

Table 10 clearly demonstrates the main distinctive features of the EAFD processing using the Waelz process and the calcination with lime. Besides the above-mentioned advantages in costs due to reduced temperature and avoidance of a halogen removal stage of the EAFD calcination with lime, it generates 6–8 times less sublimate than the Waelz process that allows to use a simpler gas cleaning system. On the other hand, an approximately threefold growth of the calcine amount compared to the Waelz oxide is expected that requires a corresponding increase in productivity of the next leaching stage. Additionally, it should be appreciated that the Waelz process is highly flexible for the charge feedstock of various zinc speciation including oxide, ferrite, sulfide, and sulfate, while the performance of the calcination with lime has still proved only for the EAFD containing zinc in ferrite and oxide form.

One more point to be mentioned for the EAFD calcination with lime is unclear prospect for the residue utilization after the calcination and zinc oxide leaching, regardless of solvents used. Until recent times, no specific study has been carried out to utilize such the residue. On the other hand, it is known that the Waelz slag from EAFD processing, which considered as a hazardous waste [86], is partially recycled in construction industry. However, its recycling is limited due to significant residual contents of Zn and other heavy metals that often disallow to meet the standards according to leaching tests for construction materials [87].

Taking into account the given advantages and disadvantages, we assume that the method of EAFD processing based on its calcination with lime should be considered for the construction or reconstruction of plants, which recycle

EAFD, on the same level with the Waelz process or even as a substitution of Waelz process.

Conclusions

The paper investigated in detail the chemical and mineralogical composition of EAFD and determined its phase distribution of zinc, lead, and iron. The thermodynamic calculation, as well as laboratory experiments to investigate zinc transformation from ZnFe₂O₄ into ZnO, Pb removal during the EAFD calcination with lime, and Mössbauer analysis of the calcined EAFD sample have revealed the behavior of valuable dust components. The calcination has led to the conversion of the main part of iron from ferrite and magnetite form to Ca₂Fe₂O₅. It was found that the major part of zinc transforms into ZnO during the calcination at 900–1100 °C, while its minor part remains as a substitutional impurity

Table 11 Calculated composition of EAFD using XRD pattern by RIR method

No	Entry number*	Number of peaks	I/I _{cor}	Calculated content, wt%
1	79–206 ZnO	13	5.3	25.79
2	19–629 Fe ₃ O ₄	15	4.9	23.27
3	82–1049 ZnFe ₂ O ₄	18	5.58	22.81
4	75–1573 FeMnO ₃	34	5.12	18.92
5	089–7409 Cu _{0.4} Zn _{0.6} Fe ₂ O ₄	18	5.28	3.43
6	78–751 NaCl	9	4.7	2.57
7	74–1225 MgO	5	3.04	0.97
8	41–1476 KCl	9	6.07	0.72
9	26–1080 C	14	2.73	0.51
	39–368 Ca ₃ Al ₂ (SiO ₄) ₃	39	2.33	0.51
10	72–1937 CaCO ₃	33	3.27	0.27
12	13–162 Mn ₃ O ₄	12	2.79	0.21

*Entry numbers are given from the ICDD and COD databases

Table 12 Calculated composition of the calcined EAFD sample with 30% CaO at 1000 °C for 120 min using XRD pattern by RIR method

No	Entry number*	Number of peaks	I/I_{cor}	Calculated content, wt%
1	80–75 ZnO	13	5.43	77.13
2	45–569 $\text{Ca}_2\text{Fe}_{1.7}\text{Zn}_{0.15}\text{Si}_{0.15}\text{O}_5$	27	1.6	7.97
3	71–2264 $\text{Ca}_2\text{Fe}_2\text{O}_5$	123	2.57	7.53
4	80–1274 $\text{Ca}_2\text{Cr}_{0.5}\text{Fe}_{1.5}\text{O}_5$	134	2.59	3.30
5	24–356 $\text{CuCr}_{1.7}\text{Mn}_{0.3}\text{O}_4$	11	3.3	1.23
6	77–2010 CaO	7	4.52	0.96
7	41–586 $\text{Ca}(\text{Fe},\text{Mg})(\text{CO}_3)_2$	41	2.8	0.91
8	74–1554 $(\text{Mn}_{2.58}\text{Fe}_{0.34}\text{Ca}_{0.08})(\text{Al}_{1.99}\text{Fe}_{0.01})\text{Si}_3\text{O}_{12}$	39	2.73	0.47
9	33–303 Ca_2SiO_4	28	1.36	0.33
10	19–943 K_2CaSiO_4	14	1.4	0.17

*Entry numbers are given from the ICDD databases

of dicalcium ferrite. At the same time, the main part of lead vaporizes both as chlorides and $\text{PbO}_{(\text{g})}$; the primary

mechanism of lead evaporation depends on the calcination temperature and EAFD composition.

The optimal calcination conditions, which led to obtaining 90.2% Zn in free oxide form, as well as volatilization of 87% Pb and 95% Cl, are as follows: EAFD:CaO mass ratio is 1: 0.3, the temperature is 1000 °C, and the duration is 120 min.

Appendix

Tables 11 and 12 list the composition of EAFD and the calcined EAFD, respectively, according to the XRD data. The Tables include entry numbers from the XRD databases, a number of peaks within a range from 10 to 90° of the 2-theta angles, and I/I_{cor} values used for the calculation of the mass composition. It should be noted that the presented results are rough due to a number of RIR method limitations, which include the possibility of the presence of solid solutions, non-crystalline, defective, nonstoichiometric or unidentified

Fig. 13 Mössbauer spectra of the EAFD sample calcined with 30% CaO at 1000 °C for 120 min, models for their description (the spectra were fitted under conditions of full diagonalization of the hyperfine Hamiltonian), and the corresponding hyperfine magnetic field probability distribution functions

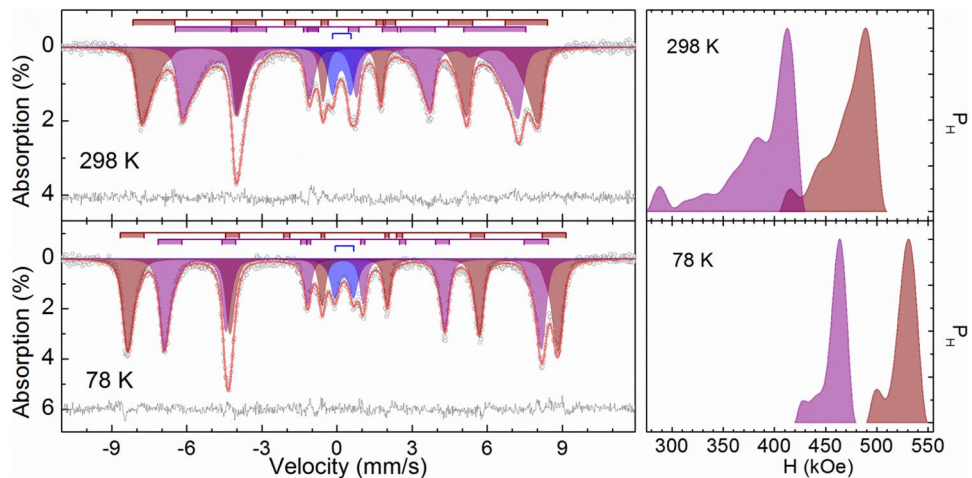


Table 13 Parameters of the Mössbauer spectra of the calcined EAFD sample with 30% CaO at 1000 °C for 120 min (the spectra were fitted under conditions of full diagonalization of the hyperfine Hamiltonian)

Tempera- ture, K		296								78							
Site	#	δ^* mm/s	$\Delta E_q (\Delta)$	Γ_{exp}	H_{max} kOe	H	Θ °	φ	S#	δ mm/s	$\Delta E_q (\Delta)$	Γ_{exp}	H_{max} kOe	η	Θ °	φ	S#
$\text{Fe}^{3+}_{\text{Oh}}$	1	0.360	1.32	0.268	489.1	0.25	90	0	43.1	0.476	1.20	0.315	531.1	0.20	90	0	47.0
$\text{Fe}^{3+}_{\text{Th}}$	2	0.192	-1.425	0.32	412.6	0.00	90	0	48.4	0.289	-1.42	0.314	463.9	0.00	90	0	44.3
$\text{Fe}^{3+}_{\text{Th}}$	3	0.184	(0.727)	0.432					8.5	0.290	(0.749)	0.438					8.7

* δ – isomer shift, $\Delta E_q (\Delta)$ – quadrupole splitting, Γ_{exp} – line width, H_{max} – hyperfine magnetic field for maximum of mode distribution functions, $\eta = (V_{xx} - V_{yy})/V_{zz}$ – asymmetry parameter, $\theta (\varphi)$ – the polar angle between V_{zz} (V_{xx}) and the direction of the internal magnetic field H_{hf} , and S# – relative area of a subspectrum #.

phases, incompleteness of the XRD databases, and so on. Apparently, chemical methods are more reliable.

Figure 13 and Table 13 demonstrate the Mössbauer spectrum and their parameters, respectively, of the calcined EAFD at 1000 °C for 120 min with 30% CaO fitted under conditions of full diagonalization of the hyperfine Hamiltonian.

Acknowledgements The authors appreciate the Chemical Analytical Laboratory of the JSC “Design & Survey and Research & Development Institute of Industrial Technology” for chemical analysis, as well as the Analytical Department of A.A. Baikov Institute of Metallurgy and Materials Science, Russian Academy of Science for the analysis of chlorine. The authors would like to express profound appreciation to Artem Semenov, Darya Grigoreva, Ekaterina Zhiltsova, and Maria Panova for assistance in the experiments with EAFD.

Funding The work was carried out within Russian State Assignment No. 075–00715–22–00. D.A. Pankratov performed this study in accordance with the state assignment of Lomonosov Moscow State University “Solving of problems of nuclear energy and environmental safety problems, as well as diagnostics of materials using ionizing radiation” (Project Reg. No. 122030200324-1).

Declarations

Conflict of Interest The authors declare that they have no conflict of interest.

References

- World Steel Association (2021) World steel in figures. <https://worldsteel.org/wp-content/uploads/Steel-Statistical-Yearbook-2020-concise-version.pdf>. Accessed 15 March 2022
- Alves EO, Amaro DRA, Silva ECO et al (2018) Study on effect of EAFD particulate reinforcement in AA7075 aluminum matrix composites. *Mater Res* 21:e20170779. <https://doi.org/10.1590/1980-5373-mr-2017-0779>
- Jorge J (2015) Secondary zinc as part of the supply chain and the rise of EAF dust recycling. In: ILZSG 19th zinc & its markets seminar. Helsinki, Finland. 6 May 2015
- Suetens T, Guo M, Van Acker K, Blanpain B (2015) Formation of the ZnFe₂O₄ phase in an electric arc furnace off-gas treatment system. *J Hazard Mater* 287:180–187. <https://doi.org/10.1016/j.jhazmat.2015.01.050>
- Chen WS, Shen YH, Tsai MS, Chang FC (2011) Removal of chloride from electric arc furnace dust. *J Hazard Mater* 190:639–644. <https://doi.org/10.1016/j.jhazmat.2011.03.096>
- Menad N, Ayala JN, Garcia-Carcedo F et al (2003) Study of the presence of fluorine in the recycled fractions during carbothermal treatment of EAF dust. *Waste Manag* 23:483–491. [https://doi.org/10.1016/S0956-053X\(02\)00151-4](https://doi.org/10.1016/S0956-053X(02)00151-4)
- Sinclair RJ (2005) The extractive metallurgy of zinc, 1st edn. Australasian Institute of Mining and Metallurgy, Carlton Victoria
- Wu X, Liu Z, Liu X (2013) Chloride ion removal from zinc sulfate aqueous solution by electrochemical method. *Hydrometallurgy* 134–135:62–65. <https://doi.org/10.1016/j.hydromet.2013.01.017>
- Hu Y, Wang H, Wang Y, Wang H (2018) Simultaneous removal of fluorine and chlorine from zinc sulfate solution in iron precipitation process. *J Sustain Metall* 4:95–102. <https://doi.org/10.1007/s40831-017-0154-0>
- Mamyachenkov SV, Kolmachikhina EB, Bludova DI, Anisimova OS (2020) Choice of a sorbent for purification of sulfate zinc solutions from fluorine ions. *Russ J Non-Ferrous Met* 61:475–481. <https://doi.org/10.3103/S1067821220050090>
- Shao S, Ma B, Wang C et al (2022) A review on the removal of magnesium and fluoride in zinc hydrometallurgy. *J Sustain Metall* 8:25–36. <https://doi.org/10.1007/s40831-022-00500-4>
- Lin X, Peng Z, Yan J et al (2017) Pyrometallurgical recycling of electric arc furnace dust. *J Clean Prod* 149:1079–1100. <https://doi.org/10.1016/j.jclepro.2017.02.128>
- Binnemans K, Jones PT, Manjón Fernández Á, Masaguer Torres V (2020) Hydrometallurgical processes for the recovery of metals from steel industry by-products: a critical review. *J Sustain Metall* 6:505–540. <https://doi.org/10.1007/s40831-020-00306-2>
- Kozlov PA (2003) The Waelz process. *Ore and Metals* PH, Moscow
- Buitrago Hernández LJ, Prada ID, Amaral-Labat G et al (2018) Microstructural, thermochemistry and mechanical evaluation of self-reducing pellets using electric arc furnace (EAF) dust containing zinc for Waelz process. *Rev Mater* 23:1–13. <https://doi.org/10.1590/s1517-707620180002.0343>
- Morcali MH, Yucel O, Aydin A, Derin B (2012) Carbothermic reduction of electric arc furnace dust and calcination of Waelz oxide by semi-pilot scale rotary furnace. *J Min Metall Sect B Metall* 48:173–184. <https://doi.org/10.2298/JMMB111219031M>
- Degtyarev AM, Ivakin DA, Shumilin YP, Mayorov SP (2015) Mastering of technology of waelz-oxide calcination in pipe rotary furnace. *Tsvetnye Met* 5:31–35. <https://doi.org/10.17580/tsm.2015.05.06>
- Ding YC, Chih-Chien L, Cheng TW (2015) The purification of crude zinc oxide using scrubbing, magnetic separation, and leaching processes. *Sep Sci Technol* 50:2405–2414. <https://doi.org/10.1080/01496395.2015.1052884>
- Iliev P, Stefanova V, Lucheva B, Kolev D (2017) Purification of zinc containing Waelz oxides from chlorine and fluorine. *J Chem Technol Metall* 52:252–257
- Ruetten J (2006) Application of the Waelz Technology on resource recycling of steel mill dust. *SEAISI Q* 35:14–17
- Office of Air and Radiation, U.S. Environmental Protection Agency (2009) Technical support document for the zinc production sector: proposed rule for mandatory reporting of greenhouse gases. <https://www.epa.gov/sites/production/files/2015-07/documents/zincproductiontsd.pdf>. Accessed 28 June 2022
- Ariyama T, Takahashi K, Kawashiri Y, Nouchi T (2019) Diversification of the ironmaking process toward the long-term global goal for carbon dioxide mitigation. *J Sustain Metall* 5:276–294. <https://doi.org/10.1007/s40831-019-00219-9>
- Wang X, Wei Y, Shao Q (2020) Decomposing the decoupling of CO₂ emissions and economic growth in China’s iron and steel industry. *Resour Conserv Recycl* 152:104509. <https://doi.org/10.1016/j.resconrec.2019.104509>
- Attahiru YB, Aziz MMA, Kassim KA et al (2019) A review on green economy and development of green roads and highways using carbon neutral materials. *Renew Sustain Energy Rev* 101:600–613. <https://doi.org/10.1016/j.rser.2018.11.036>
- Chairaksa-Fujimoto R, Inoue Y, Umeda N et al (2015) New pyrometallurgical process of EAF dust treatment with CaO addition. *Int J Miner Metall Mater* 22:788–797. <https://doi.org/10.1007/s12613-015-1135-6>
- Lv W, Gan M, Fan X et al (2019) Mechanism of calcium oxide promoting the separation of zinc and iron in metallurgical dust under reducing atmosphere. *J Mater Res Technol* 8:5745–5752. <https://doi.org/10.1016/j.jmrt.2019.09.043>
- Polsilapa S, Sriyowong N (2015) Electric arc furnace dust treatment by the combination of pyro/hydrometallurgical processes.

- Appl Mech Mater 799–800:72–76. <https://doi.org/10.4028/www.scientific.net/amm.799-800.72>
28. Xie Z, Guo Y, Jiang T et al (2017) The extraction of zinc from zinc ferrite by calcified-roasting and ammonia-leaching process. In: Hwang J, Jiang T, Kennedy MW, et al. (eds) 8th international symposium on high-temperature metallurgical processing. The Minerals, Metals & Materials Series. Springer, Cham, pp 485–493
 29. Yakornov SA et al (2017) Thermodynamic analysis of zinc ferrite decomposition in electric arc furnace dust by lime. Russ J Non-Ferrous Met 58:586–590. <https://doi.org/10.3103/S1067821217060165>
 30. Yakornov SA, Panshin AM, Grudinsky PI et al (2018) Method of electric arc furnace dust processing by calcination with lime with following alkaline leaching. Russ Metall 2018:1282–1287. <https://doi.org/10.1134/S0036029518130268>
 31. Roine A (2019) HSC Chemistry® software, version 9.9, Outotec, Pori, Finland. <https://www.outotec.com/HSC>. Accessed 23 May 2020
 32. Filippova NA (1975) The phase analysis of ores and their processing products, 2nd edn. Himiya, Moscow
 33. Mesquita RBR, Fernandes SMV, Rangel AOSS (2002) Turbidimetric determination of chloride in different types of water using a single sequential injection analysis system. J Environ Monit 4:458–461. <https://doi.org/10.1039/b200456a>
 34. Gates-Rector S, Blanton T (2019) The powder diffraction file: a quality materials characterization database. Powder Diffr 34:352–360. <https://doi.org/10.1017/S0885715619000812>
 35. Vaitkus A, Merkys A, Grazulis S (2021) Validation of the crystallography open database using the crystallographic information framework. J Appl Crystallogr 54:661–672. <https://doi.org/10.1107/S1600576720016532>
 36. Jones DH, Srivastava KKP (1986) Many-state relaxation model for the Mössbauer spectra of superparamagnets. Phys Rev B 34:7542–7548. <https://doi.org/10.1103/PhysRevB.34.7542>
 37. Pankratov DA, Anuchina MM (2019) Nature-inspired synthesis of magnetic non-stoichiometric Fe₃O₄ nanoparticles by oxidative in situ method in a humic medium. Mater Chem Phys 231:216–224. <https://doi.org/10.1016/j.matchemphys.2019.04.022>
 38. Oh SJ, Cook DC, Townsend HE (1998) Characterization of iron oxides commonly formed as corrosion products on steel. Hyperfine Interact 112:59–66
 39. Pankratov DA, Anuchina MM, Spiridonov FM, Krivtsov GG (2020) Fe₃₋₈O₄ nanoparticles synthesized in the presence of natural polyelectrolytes. Crystallogr Reports 65:393–397. <https://doi.org/10.1134/S1063774520030244>
 40. Klygach DS, Vakhitov MG, Pankratov DA et al (2021) MCC: Specific of preparation, correlation of the phase composition and electrodynamic properties. J Magn Magn Mater 526:167694. <https://doi.org/10.1016/j.jmmm.2020.167694>
 41. Adolphi NL, Huber DL, Bryant HC et al (2010) Characterization of single-core magnetite nanoparticles for magnetic imaging by SQUID relaxometry. Phys Med Biol 55:5985–6003. <https://doi.org/10.1088/0031-9155/55/19/023>
 42. Nadeem K, Krenn H, Traussnig T et al (2011) Effect of dipolar and exchange interactions on magnetic blocking of maghemite nanoparticles. J Magn Magn Mater 323:1998–2004. <https://doi.org/10.1016/j.jmmm.2011.02.041>
 43. Iqbal MJ, Yaqub N, Sepiol B, Ismail B (2011) A study of the influence of crystallite size on the electrical and magnetic properties of CuFe₂O₄. Mater Res Bull 46:1837–1842. <https://doi.org/10.1016/j.materresbull.2011.07.036>
 44. Patil VU, Kulkarni RG (1979) Magnetic properties of CuZn ferrite investigated by Mössbauer spectroscopy. Solid State Commun 31:551–555. [https://doi.org/10.1016/0038-1098\(79\)90251-5](https://doi.org/10.1016/0038-1098(79)90251-5)
 45. Ata-Allah SS, Hashhash A (2006) Jahn-Teller effect and superparamagnetism in zn substituted copper-gallate ferrite. J Magn Magn Mater 307:191–197. <https://doi.org/10.1016/j.jmmm.2006.04.002>
 46. Siddique M, Khan RTA, Shafi M (2008) Fluctuation in occupancy of Cu²⁺ ions in Zn- and Cd-substituted Cu-ferrites. J Radioanal Nucl Chem 277:531–537. <https://doi.org/10.1007/s10967-007-7048-8>
 47. Le Roux H (1990) A Mossbauer study of paramagnetic and magnetic components in an uncalcined iron manganese oxide powder. J Phys Condens Matter 2:3391–3398. <https://doi.org/10.1088/0953-8984/2/14/023>
 48. Seifu D, Kebede A, Oliver FW et al (2000) Evidence of ferrimagnetic ordering in FeMnO₃ produced by mechanical alloying. J Magn Magn Mater 212:178–182. [https://doi.org/10.1016/S0304-8853\(99\)00787-8](https://doi.org/10.1016/S0304-8853(99)00787-8)
 49. Rayaprol S, Ribeiro RAP, Singh K et al (2019) Experimental and theoretical interpretation of magnetic ground state of FeMnO₃. J Alloys Compd 774:290–298. <https://doi.org/10.1016/j.jallcom.2018.09.367>
 50. Li FS, Wang L, Wang JB et al (2004) Site preference of Fe in nanoparticles of ZnFe₂O₄. J Magn Magn Mater 268:332–339. [https://doi.org/10.1016/S0304-8853\(03\)00544-4](https://doi.org/10.1016/S0304-8853(03)00544-4)
 51. Grudinsky P, Pankratov D, Kovalev D et al (2021) Comprehensive study on the mechanism of sulfating roasting of zinc plant residue with iron sulfates. Materials (Basel) 14:5020. <https://doi.org/10.3390/ma14175020>
 52. Kazanbaev LA, Kozlov PA, Kubasov VL, Kolesnikov AV (2006) Zinc hydrometallurgy (cleaning of solutions and electrolysis). Ore and Metals PH, Moscow
 53. Yoo J-M, Kim B-S, Lee J et al (2005) Kinetics of the volatilization removal of lead in electric arc furnace dust. Mater Trans 46:323–328. <https://doi.org/10.2320/matertrans.46.323>
 54. Wang N, Jin AJ, Chen M (2006) Chlorination-vaporization reaction of Pb-oxychloride in pyrometallurgical recycling process of dust and ash. Dev Chem Eng Miner Process 14:385–396. <https://doi.org/10.1002/apj.5500140306>
 55. Shapter JG, Brooker MH, Skinner WM (2000) Observation of the oxidation of galena using Raman spectroscopy. Int J Miner Process 60:199–211. [https://doi.org/10.1016/S0301-7516\(00\)00017-X](https://doi.org/10.1016/S0301-7516(00)00017-X)
 56. Habashi F (1986) Principles of extractive metallurgy: volume 3: Pyrometallurgy, 1st edn. CRC Press, New York
 57. Li Y, Yang S, Taskinen P et al (2019) Cleaner recycling of spent lead-acid battery paste and co-treatment of pyrite cinder via a reductive sulfur-fixing method for valuable metal recovery and sulfur conservation. Metals (Basel) 9:911. <https://doi.org/10.3390/met9080911>
 58. Risold D, Nagata J-I (1998) Thermodynamic description of the Pb-O system. J Phase Equilibria 19:213–233. <https://doi.org/10.1361/105497198770342238>
 59. Abbas T, Godoy S, Hassan S, Lockwood FC (1996) The effects of extraneous metal oxides and chlorides on the partitioning of toxic metals in the flames of a pulverised waste fuel. Combust Sci Technol 121:281–298. <https://doi.org/10.1080/00102209608935599>
 60. Jakob A, Stucki S, Kuhn P (1995) Evaporation of heavy metals during the heat treatment of municipal solid waste incinerator fly ash. Environ Sci Technol 29:2429–2436. <https://doi.org/10.1021/es00090a040>
 61. Jakob A, Stucki S, Struis RPWJ (1996) Complete heavy metal removal from fly ash by heat treatment: influence of chlorides on evaporation rates. Environ Sci Technol 30:3275–3283. <https://doi.org/10.1021/es960059z>
 62. Eibschütz M, Ganiel U, Shtrikman S (1969) Mössbauer and magnetic studies of dicalcium ferrite (Ca₂Fe₂O₅). J Mater Sci 4:574–580. <https://doi.org/10.1007/BF00550113>

63. Shaula AL, Pivak YV, Waerenborgh JC et al (2006) Ionic conductivity of brownmillerite-type calcium ferrite under oxidizing conditions. *Solid State Ionics* 177:2923–2930. <https://doi.org/10.1016/j.ssi.2006.08.030>
64. Kagomiya I, Hirota Y, Kakimoto KI et al (2017) Weak ferromagnetic ordering in brownmillerite $\text{Ca}_2\text{Fe}_2\text{O}_5$ and its effect on electric field gradients. *Phys Chem Chem Phys* 19:31194–31201. <https://doi.org/10.1039/c7cp04520d>
65. Yamauchi S, Kurimoto Y, Takayama T, Sakai Y (2020) Mössbauer and Raman characterization of ash produced by burning ancient buried Japanese cedar and investigation for its unusual color tone. *J Radioanal Nucl Chem* 326:753–764. <https://doi.org/10.1007/s10967-020-07359-3>
66. Colville AA, Geller S (1971) The crystal structure of brownmillerite, $\text{Ca}_2\text{FeAlO}_5$. *Acta Crystallogr Sect B* 27:2311–2315. <https://doi.org/10.1107/s056774087100579x>
67. Abe N, Khanh ND, Sasaki T, Arima T (2014) Magnetic-field-induced spin flop transition and magnetoelectric effect in $\text{Ca}_2\text{Fe}_{2-x}\text{Al}_x\text{O}_5$. *Phys Rev B* 89:054437. <https://doi.org/10.1103/PhysRevB.89.054437>
68. Bertaut EF, Blum P, Sagnières A (1959) Structure du ferrite bicalcique et de la brownmillerite. *Acta Crystallogr* 12:149–159. <https://doi.org/10.1107/s0365110x59000433>
69. Valeev D, Zinoveev D, Kondratiev A et al (2020) Reductive smelting of neutralized red mud for iron recovery and produced pig iron for heat-resistant castings. *Metals (Basel)*. <https://doi.org/10.3390/met10010032>
70. Onodera H, Fujita A, Yamamoto H et al (1987) Mössbauer study of the intermetallic compound $\text{Nd}_2\text{Fe}_{14}\text{B}$. I. interpretation of complex spectrum. *J Magn Magn Mater* 68:6–14. [https://doi.org/10.1016/0304-8853\(87\)90090-4](https://doi.org/10.1016/0304-8853(87)90090-4)
71. Rykov A, Gaignaert V, Van Tendello G et al (1994) Structural aspects and antiferromagnetic ordering in the “123” derivative $\text{LnSr}_2\text{Cu}_2\text{Ga}_{1-x}\text{Fe}_x\text{O}_{7-8}$ ($\text{Ln} = \text{Y, Ho}$). *J Solid State Chem* 113:94–108. <https://doi.org/10.1006/jssc.1994.1346>
72. Stahl QE, Redhammer GJ, Tippelt G, Reyer A (2019) Structural and spectroscopic characterization of the brownmillerite-type $\text{Ca}_2\text{Fe}_{2-x}\text{Ga}_x\text{O}_5$ solid solution series. *Phys Chem Miner* 46:271–298. <https://doi.org/10.1007/s00269-018-1003-9>
73. Grant RW, Wiedersich H, Geller S et al (1967) Magnetic properties of substituted $\text{Ca}_2\text{Fe}_2\text{O}_5$. *J Appl Phys* 38:1455–1456. <https://doi.org/10.1063/1.1709664>
74. Grenier J-C, Pouchard M, Hagenmuller P (1976) Evaluation des interactions magnetiques dans les phases derivees du ferrite bicalcique $\text{Ca}_2\text{Fe}_2\text{O}_5$. *Mater Res Bull* 11:721–730. [https://doi.org/10.1016/0025-5408\(76\)90151-3](https://doi.org/10.1016/0025-5408(76)90151-3)
75. Pankratov DA, Yurev AI (2013) Mössbauer diagnostics of the isomorphic substitution of iron for aluminum in triclinic iron vanadate. *Bull Russ Acad Sci Phys* 77:759–764. <https://doi.org/10.3103/S1062873813060221>
76. Grenier JC, Pouchard M, Hagenmuller P (1975) Influence de la substitution du fer sur les proprietes magnetiques des solutions solides $\text{Ca}_2\text{Fe}_{2-x}\text{M}_x\text{O}_5$ ($\text{M} = \text{Al, Sc, Cr Co, Ga}$). *J Solid State Chem* 13:92–98. [https://doi.org/10.1016/0022-4596\(75\)90085-7](https://doi.org/10.1016/0022-4596(75)90085-7)
77. Gibb TC, Matsuo M (1990) A study of microdomain formation and structural intergrowth in the oxygen-deficient perovskite $\text{Ca}_2\text{Fe}_{2-x}\text{Cr}_x\text{O}_{5+y}$ by Mössbauer spectroscopy. *J Solid State Chem* 88:485–487. [https://doi.org/10.1016/0022-4596\(90\)90245-S](https://doi.org/10.1016/0022-4596(90)90245-S)
78. Zöttl M, Pöllmann H (2006) Stability and properties of brownmillerites $\text{Ca}_2(\text{Al, Mn, Fe})_2\text{O}_5$ and perovskites $\text{Ca}(\text{Mn, Fe})\text{O}_{3-x}$ in the system $\text{Ca}_2\text{Fe}_2\text{O}_5$ – $\text{Ca}_2\text{Mn}_2\text{O}_5$ – $\text{Ca}_2\text{Al}_2\text{O}_5$. *J Am Ceram Soc* 89:3491–3497. <https://doi.org/10.1111/j.1551-2916.2006.01242.x>
79. Rykov AI, Nomura K, Ueda Y, Vasiliev AN (2008) An Ising ferrimagnet with layered and chained magnetic sublattices: $\text{Ca}_2\text{FeMnO}_5$. *J Magn Magn Mater* 320:950–956. <https://doi.org/10.1016/j.jmmm.2007.09.018>
80. Pankratov DA (2014) Mössbauer study of oxo derivatives of iron in the Fe_2O_3 – Na_2O_2 system. *Inorg Mater* 50:82–89. <https://doi.org/10.1134/S0020168514010154>
81. Suzuki K, Ito S, Nishikawa T (1986) Effect of Na, K and Fe on the formation of α - and β - Ca_2SiO_4 . *Cem Concr Res* 16:885–892. [https://doi.org/10.1016/0008-8846\(86\)90012-8](https://doi.org/10.1016/0008-8846(86)90012-8)
82. Nishida T, Kubuki S, Oka N (2021) Local structure, glass transition, structural relaxation, and crystallization of functional oxide glasses investigated by Mössbauer spectroscopy and DTA. *J Mater Sci Mater Electron* 32:23655–23689. <https://doi.org/10.1007/s10854-021-06855-w>
83. Newbury DE (2002) Microanalysis for low voltage scanning electron microscopy. *J Res Natl Inst Stand Technol* 107:605–619. <https://doi.org/10.6028/jres.107.049>
84. Yakornov SA, Panshin AM, Kozlov PA, Ivakin DA (2017) Development of technology and instrumental scheme of pyrometallurgical processing of ferrous metallurgy dusts. *Tsvetnye Met* 9:39–44. <https://doi.org/10.17580/tsm.2017.09.06>
85. International Energy Agency (2009) CO_2 emissions from fuel combustion. 2020 edition. https://iea.blob.core.windows.net/assets/474cf91a-636b-4fde-b416-56064e0c7042/WorldCO2_Documentation.pdf. Accessed 28 June 2022
86. Cifrian E, Coronado M, Quijorna N et al (2019) Waelz slag-based construction ceramics: effect of the trial scale on technological and environmental properties. *J Mater Cycles Waste Manag* 21:1437–1448. <https://doi.org/10.1007/s10163-019-00896-4>
87. Grudinsky PI, Zinoveev DV, Dyubanov VG, Kozlov PA (2019) State of the art and prospect for recycling of waelz slag from electric arc furnace dust processing. *Inorg Mater Appl Res* 10:1220–1226. <https://doi.org/10.1134/S2075113319050071>

Publisher's Note Springer Nature remains neutral with regard to jurisdictional claims in published maps and institutional affiliations.